

Constrained Simulations of the Real Universe: II. Observational Signatures of Intergalactic Gas in the Local Supercluster Region

Andrey V. Kravtsov¹

Department of Astronomy, The Ohio State University, 140 West 18th Ave., Columbus, OH 43210-1173

Anatoly Klypin

Astronomy Department, New Mexico State University, Las Cruces, NM 88003-0001

Yehuda Hoffman

The Racah Inst. of Physics, Hebrew University, Jerusalem 91904, Israel

ABSTRACT

We present results of gasdynamics+ N -body *constrained* cosmological simulations of the Local Supercluster region (LSC; about $30h^{-1}$ Mpc around the Virgo cluster), which closely mimic the real Universe within 100 Mpc by imposing constraints from MARK III catalog of galaxy peculiar velocities. The simulations are used to study the properties and possible observational signatures of intergalactic medium in the LSC region. We find that, in agreement with previous unconstrained simulations, $\approx 30\%$ of the gas in this region is in the warm/hot phase at $T \sim 10^5 - 10^7$ K, and $\approx 40\%$ in the diffuse phase at $T < 10^5$ K in low-density regions. The X-ray emission from the warm/hot gas may represent a small ($\sim 5 - 10\%$) but important contribution to the X-ray background observed by the ROSAT All-Sky Survey at energies around 1 keV. The best prospects for detection of the warm/hot intergalactic medium of the LSC located in filaments and in the vicinity of virialized regions of groups and clusters are through absorption in resonant lines of OVII and OVIII in soft X-rays and in the OVI doublet in UV. If intergalactic gas in filaments ($\rho/\langle\rho\rangle \sim 1 - 10$) is enriched to typical metallicities of $\gtrsim 0.05$, the column densities of OVI, OVII, and OVIII along a random line of sight near the North Galactic Pole, especially near the supergalactic plane, have a significant probability to be in the range detectable by the current (*FUSE*, *XMM*) and future (*Constellation-X*) instruments.

Subject headings: cosmology:theory – large-scale structure – methods: numerical

1. Introduction

At the present epoch baryons in stars and galaxies constitute only a small fraction of the total baryon density predicted by the Big Bang nucleosynthesis model (Fukugita, Hogan, & Peebles 1998). This is in agreement with the Cold Dark Matter (CDM) models of structure forma-

tion which predict that a large fraction of baryons at $z \approx 0$ is located in filaments and intergalactic medium of groups and clusters, where it is shock-heated to temperatures of $T \sim 10^5 - 10^7$ K (Cen & Ostriker 1999b; Davé et al. 1999).

The detection of the warm/hot intergalactic medium (WHIM) and studies of its properties represent a challenge. The integrated soft X-ray emission of this gas may contribute significantly to the observed extragalactic X-ray background (XRB; e.g., Croft et al. 2001; Phillips et al. 2001; Voit

¹Hubble Fellow; *Current address:* Department of Astronomy & Astrophysics, University of Chicago, 5640 S. Ellis Ave., Chicago, IL 60637, US

& Bryan 2001). The best prospects for direct detection are, however, through absorption or emission in the lines of ionic species of heavy elements such as oxygen, which requires very sensitive X-ray and UV spectroscopy of bright background sources (Shapiro & Bahcall 1980; Basko et al. 1981; Aldcroft et al. 1994; Hellsten et al. 1998; Perna & Loeb 1998; Fang & Canizares 2000). The recent launches of new generation X-ray (*Chandra* and *XMM-Newton*) and UV (*FUSE*) satellites, as well as access to the UV wavelengths with the *Hubble Space Telescope* (*HST*), led to first detections of absorption in the resonance OVI doublet in UV at both low (Tripp & Savage 2000; Tripp et al. 2000) and intermediate (Reimers et al. 2001) redshifts. The first attempt to detect resonance line absorption of heavy metals in soft X-rays with *Chandra* by Fang et al. (2001) yielded only an upper limit, but more sensitive studies are currently underway.

Spectroscopic studies of the warm/hot medium are very promising for understanding properties and evolution of this important baryonic component. An important piece of information is the state of the WHIM gas in the nearby Universe at $z = 0$. However, the absorption at very low redshifts should be due to only a few large-scale structures and one would therefore expect model predictions to be rather uncertain due to the cosmic variance. Moreover, we know that the Local Group is surrounded by the large-scale filamentary structures in the density field such as the Local Supercluster, Perseus-Pisces supercluster, the Great Attractor, etc. They are expected to contain warm/hot gas and could serve as targets for its detection. It would be interesting therefore to explore observational signatures of this gas and make theoretical predictions on the sky coverage and column density distributions of gas in these structures.

Fortunately, this problem can be addressed by using *constrained simulations* (Klypin et al. 2001a, hereafter Paper I), i.e., cosmological simulations with initial conditions constrained to reproduce the observed large-scale structures in the nearby Universe (see also Kolatt et al. 1996; Bistolos & Hoffman 1998; van de Weygaert & Hoffman 1999). The initial conditions are generated within the framework of a flat CDM cosmogony by means of constrained realizations of Gaussian fields, where the constraints are set by the MARK III survey of

peculiar velocities. The setup of these realizations is such that that the structure on scales larger than a few Mpc is tightly constrained by the data, while smaller scales essentially constitute a random realization of the assumed primordial perturbation field.

In the study presented here, we used the method of Klypin et al. (2001a) to set up and run constrained N -body+gasdynamics simulations of the Local Supercluster region (LSC; a roughly spherical region of $R \lesssim 30h^{-1}\text{Mpc}$ centered on the Virgo cluster) in ΛCDM cosmology. The simulation followed gasdynamics of the baryonic component and collisionless dynamics of dark matter particles using a newly developed eulerian adaptive mesh refinement code (see § 2). Gas cooling (except for adiabatic expansion) was not included. The main results of our study depend on the physics of shock-heated ($T \gtrsim 10^5$ K) gas in the relatively low density ($\rho/\langle\rho\rangle \sim 1 - 10$) regions. The cooling time of such gas is $t_{\text{cool}} \approx 3.1 \times 10^{11} \text{ yrs K}^{-1} \Lambda_{-23} (1 + \delta)^{-1} T_5$, where we assumed $\Omega_b = 0.02h^{-2}$ and complete ionization of gas, Λ_{-23} is cooling rate in units of $10^{-23}\text{cm}^3 \text{ erg s}^{-1}$, δ is gas overdensity, and T_5 is gas temperature in 10^5 K. The cooling time is thus longer than the Hubble time in our regions of interest and effects of cooling can be neglected. The cooling time can be short in the cluster cores where gas cooling can result in a cooling flow. Such regions, however, occupy a very small fraction of the volume and will not affect the main conclusions of the paper about the probability for the WHIM detection via metal absorption. The cooling will affect our results on the X-ray fluxes from regions in the cluster cores; our fluxes should be viewed as an upper limit on the possible emission.

The use of observational constraints dictates that the simulations are initialized and evolved in the supergalactic coordinates used to map the actual universe. This enables us to construct sky maps of the desired quantities (e.g., X-ray surface brightness, or column densities) corresponding to real objects and actual locations in the real universe. The large angular extent of the LSC and its favorable orientation on the sky² imply that a

²The concentration of nearby galaxies along the supergalactic plane extends over more than 100° . The plane is almost perpendicular to the galactic plane; its center, the Virgo cluster, is close to the North Galactic Pole.

large fraction of observational lines-of-sight in the northern galactic hemisphere pass through the regions of high gas density. We analyze the distribution and properties of gas in the LSC region focusing on its possible observational signatures such as absorption and emission by OVI, OVII, and OVIII, soft X-ray emission, and Sunyaev-Zeldovich effect.

The paper is organized as follows. The numerical code, initial conditions and simulations are described in § 2 and § 3, respectively. The geometry of density field, properties of gas in the simulation, sky maps of various quantities, and observational signatures of the gas are discussed in § 4. We conclude the paper with a brief discussion of the results and our conclusions in § 5.

2. Numerical code

The adaptive refinement tree (ART) code (Kravtsov et al. 1997; Kravtsov 1999) achieves high spatial resolution by adaptively refining regions of interest using an automated refinement algorithm. The N -body part of the code was used extensively to run high-resolution dissipationless cosmological simulations (e.g., Kravtsov 1999, and references therein). Due to the use of eulerian mesh hierarchy in the ART algorithm, the inclusion of eulerian gasdynamics is a natural extension. The adaptive mesh refinement methods for numerical hydrodynamics enjoy widespread popularity in the physics and engineering communities and are now also gaining popularity in cosmology and astrophysics (e.g., Truelove et al. 1998; Norman & Bryan 1999; Khokhlov et al. 1999; Abel et al. 2000; Plewa & Müller 2001; Refregier & Teyssier 2001; Ricker 2001). The adaptive mesh refinement is particularly attractive for cosmology because interesting regions in cosmological simulations usually occupy only a small fraction of the computational volume and thus can be refined with relatively small number of mesh cells.

Here we will briefly describe the gasdynamics part of the algorithm, detailed account of which will be presented elsewhere (see also Kravtsov 1999). The equations of gasdynamics and particle motion are integrated in “supercomoving” variables (Shandarin 1980; Martel & Shapiro 1998). These variables are remarkable as their use almost completely (completely for ideal gas with $\gamma = 5/3$)

eliminates explicit dependence on cosmology in the model equations. The equations can therefore be integrated using standard gravitation and gasdynamics solvers with no need for additional coefficients and corrections.

A simulation is usually started with a uniform grid covering the entire computational domain. As the universe evolves and expands, additional resolution is required in and around dense objects. The ART code uses mesh refinement to increase spatial resolution in regions where such increase is needed. The refinements are recursive: the refined regions can also be refined, each subsequent refinement having half of the previous level’s cell size. This creates a hierarchy of refinement meshes of different resolution, size, and geometry covering regions of interest. Because each individual cubic cell can be refined, the shape of the refinement mesh can be arbitrary and effectively match the geometry of the region of interest. This strategy is particularly well suited for simulations of a selected region within a large computational box, as in the constrained simulations presented below.

During a simulation, spatial refinement is accompanied by temporal refinement. Namely, each level of refinement, l , is integrated with its own time step $\Delta\tau_l = \Delta\tau_0/2^l$, where $\Delta\tau_0$ is the global time step of the zeroth refinement level in the code’s time units (the code uses time variable defined as follows: $d\tau \equiv a^{-2}dt/t_0$, where t is the physical time, a is expansion factor, and t_0 is an arbitrary time constant). This variable time stepping is very important for accuracy of the results. As the force resolution increases, more steps are needed to integrate the trajectories accurately. To increase mass resolution in certain regions the code uses particles of different masses. In the simulations presented in this paper this ability was used to achieve high mass resolution inside a region centered around the Virgo cluster (see below).

The main features of the gasdynamics implementation follow closely the algorithm of Khokhlov (1998). A second-order Godunov-type solver (Colella & Glaz 1985) is used to compute numerical fluxes of gas variables through each cell interface, with “left” and “right” states estimated using linear piecewise linear reconstruction (van Leer 1979). The Riemann solver was written and kindly provided to us by A.M. Khokhlov and has good shock-capturing characteristics (Khokhlov

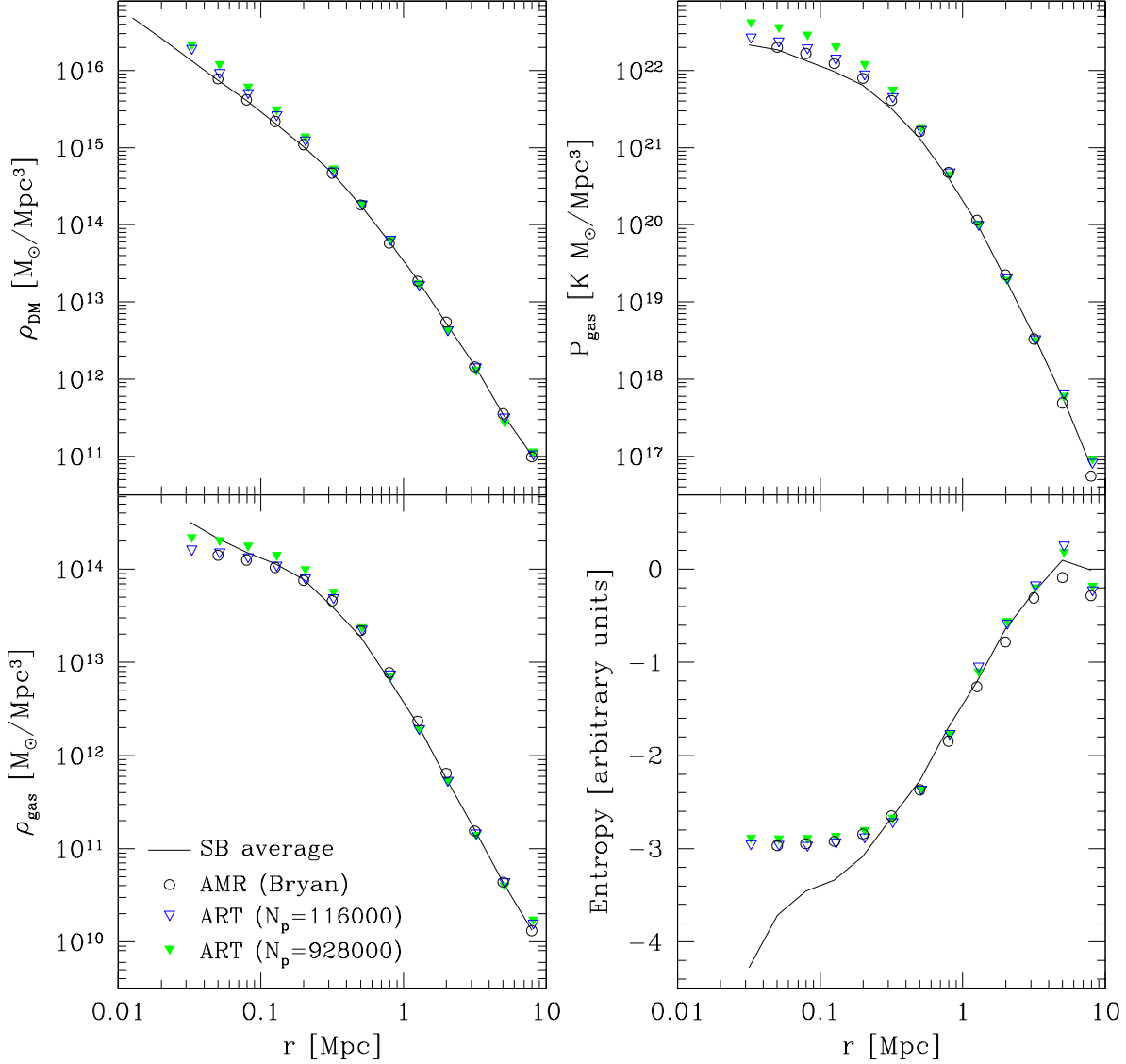


Fig. 1.— Results of the N -body+gasdynamics simulations of the “Santa Barbara” cluster using the ART code. The panels show various spherically averaged profiles; counter clockwise from the upper left: dark matter density; gas density; gas pressure; gas entropy. The ART profiles (*triangles*) are compared to the corresponding mean profiles from the SB cluster comparison project (Frenk et al. 1999) shown by the *solid line*, which represent average over 12 (13 for the ρ_{DM} profile) simulations performed using different cosmological codes. The *open circles* show profiles from the adaptive mesh refinement (AMR) simulation by Greg Bryan performed as part of the SB project. The *open triangles* show profiles for a simulation with the dark matter particle of $1 \times 10^9 M_{\odot}$ ($\approx 116,000$ particles within the cluster virial radius), while *solid triangles* show results of a simulation with eight times better mass resolution ($\approx 928,000$ particles within the virial radius). The profiles from the ART simulations are shown at scales larger than 4 formal resolutions.

1998; Kravtsov 1999) which is desirable for cosmological applications. The gasdynamics is coupled to the dynamics of dark matter through the common potential, which is used to compute accelerations for both the DM particles and the gas. The code employs the same data structures and similar refinement strategy as the previous N -body versions of the code. However, in addition to the DM density criteria it also allows for additional refinement criteria based on the local density of gas, shock, sharp gradient indicators. The refinement criteria can be combined with different weights allowing for a flexible refinement strategy that can be tuned to the need of each particular simulation.

Extensive tests of the N -body code and comparisons with other numerical N -body codes can be found in Kravtsov (1999) and Knebe et al. (2000). To compare performance of the N -body+gasdynamics code to other existing cosmological gasdynamics codes in a realistic cosmological setting, we have simulated the cluster used in the “Santa Barbara (SB) cluster comparison project” (Frenk et al. 1999). This project compared simulations of the same Coma-size cluster performed using 12 different gasdynamics codes. Figure 1 shows spherically averaged profiles of dark matter density, gas density, gas pressure, and gas entropy for the ART simulations with two different mass resolutions for the dark matter. The ART results are compared to the average profiles from the SB project and to the profile of the Adaptive Mesh Refinement (AMR) simulation³ by G.L. Bryan performed as part of the SB project. The refinements in the ART runs were based on the local gas density, with the threshold density for refinement level l equal to $4 \times \langle m_{\text{gas}} \rangle \Delta x_0^{-3l}$, where $\langle m_{\text{gas}} \rangle$ and x_0 are average gas mass per and size of zeroth-level grid cell, respectively. The simulations used 128^3 uniform grid and six levels of refinement, which corresponds to the smallest cell size of ≈ 8 kpc in the 64 Mpc computational box which is similar to the formal resolution of the AMR simulation.

The figure shows very good general agreement between the ART and Bryan’s AMR profiles, es-

³Note that this is entirely independent AMR code that uses different solvers for both gas and dark matter and different refinement algorithm.

pecially for the lower-resolution ART run which has the same mass resolution as the AMR run. The higher mass resolution run produces a somewhat steeper dark matter density profile in the innermost regions. This is in agreement with recent convergence studies for dark matter density profiles (Ghigna et al. 2000; Klypin et al. 2001b). It is interesting to note that the steepening of the DM profile affects gas profiles, resulting in a somewhat higher central gas density (and smaller core radius) and higher central temperature and pressure. The entropy profiles of the two eulerian mesh refinement simulations agree very well and show presence of a well resolved core. There is a clear and alarming mismatch of these profiles and the average SB profile which is dominated by the SPH simulations at small scales. The origin of the mismatch is unclear, although the fact that the two different eulerian codes agree well probably indicates that it is due to less accurate treatment of shocks in the SPH codes. We are currently working on more detailed comparisons of entropy evolution in ART and SPH codes.

3. Constrained simulations

The goal of this paper is to perform numerical simulations that match the observed local universe as well as possible. Namely, we are interested in reproducing the observed structures: the Virgo cluster, the Local Supercluster (LSC) and the Local Group (LG), in the approximately correct locations and embedded within the observed large-scale configuration dominated by the Great Attractor and the Perseus-Pisces supercluster.

The setup details of the constrained initial conditions used for our simulations are presented in (Klypin et al. 2001a). Initial conditions are constructed using constrained realizations based on the MARK III catalog of radial peculiar velocities and assuming the Λ CDM model with the following parameters: $\Omega_0 = 0.3$, $\Omega_\Lambda = 0.7$, $\sigma_8 = 0.9$, $\Omega_{\text{baryon}} = 0.03$, $h = 0.7$. Constrained realizations of Gaussian fields are generated by sampling the random residual from the mean (Wiener filter) field given the data and the assumed model (Hoffman & Ribak 1991). The nature of the data and the Λ CDM model implies that scales larger than a few Mpc are tightly constrained by the data while the small scale structure constitutes

a random realization of the assumed model (see Klypin et al. (2001a) for a quantitative analysis). The random (unconstrained) waves dominate on small scales which leads to random displacements of some large-scale features in the density distribution by a few Mpc from realization to realization. The realization used for our simulations was selected from a set of low-resolution dissipationless runs to have the position of the Virgo cluster to be as close to its observed location as possible. The realizations are constructed assuming that the linear theory is valid on all scales at the present epoch, and is then evolved backwards in time to the initial epoch of the simulation by the linear growth factor.

A region within a radius of $30h^{-1}\text{Mpc}$ around the Virgo cluster inside the $160h^{-1}\text{Mpc}$ computational box was selected for re-simulation at the highest mass and force resolution. The initial positions and velocities for 1024^3 particles were generated in the entire $160h^{-1}\text{Mpc}$ box (roughly centered on the Virgo cluster). Particles outside the designated high-resolution region were then merged⁴ into particles of larger mass and this process was repeated for merged particles to construct a nested hierarchy of particles of four different masses surrounding the high-resolution region. The simulation used four DM particle species with DM particle mass of $3.16 \times 10^8 h^{-1} M_\odot$ in the highest resolution region. The initial conditions used for our simulations are identical to the simulation analyzed in Klypin et al. (2001a).

The simulations presented here were run using 128^3 zeroth-level grid. The initial gas density and velocity for each grid cell was computed using DM particle positions and velocities and cloud-in-cell (CIC) interpolation. The subsequent mesh refinement was done using criteria based on the local DM and gas densities. Namely, a cell of level L is marked for refinement if mass of DM particles (evaluated using the CIC-smoothed density field) and/or mass of gas in the cell exceeds specified threshold. The final refinement map is then created by smoothing the original map using an algorithm similar to that described in Khokhlov (1998). The smoothing generally enlarges regions

⁴The larger mass (merged) particle is assigned a velocity and displacement equal to the average velocity and displacement of the smaller-mass particles.

marked for refinement and reduces noisiness of the original map. The threshold can be chosen to be different at different levels of refinement. The density-based mesh refinement is appropriate as we are interested in resolving collapsing high-density regions. However, the specific choice of threshold masses is arbitrary.

To ensure that the results of our study do not depend on the choice of thresholds, we have run two simulations with very different numerical criteria for refinement. In the first simulation (hereafter R1), the mass thresholds were the same for all levels and were set to the average mass of DM and gas per zeroth level cell ($\langle m_{\text{DM}} \rangle \approx 1.4 \times 10^{11} h^{-1} M_\odot$ and $\langle m_{\text{g}} \rangle \approx 2.3 \times 10^{10} h^{-1} M_\odot$, respectively). There was no limit on the number of refinement levels; a total of 8 levels were introduced in the highest density regions, corresponding to the smallest cell size of $\approx 4.9h^{-1}\text{kpc}$. The second simulation (hereafter R2) was started from the same initial conditions and used the same threshold masses for refinement on the zeroth and the first levels as the simulation R1. However, run R2 was limited to four levels of refinement (corresponding to the smallest cell size of $78h^{-1}\text{kpc}$ and mass thresholds for levels 2 and 3 were set to $\langle m \rangle/4$ and $\langle m \rangle/16$, respectively). The simulation R2, therefore, has lower peak resolution than the R1. The fraction of the volume resolved at the peak resolution is, however, much greater in R2 than in R1. In particular, all regions of local overdensity $\sim 20 - 30$ were refined to the peak resolution of $78h^{-1}\text{kpc}$ in R2. In the simulation R1 this resolution was reached only in regions with local overdensity higher than ~ 500 . For all the results presented in this paper there is no significant difference between simulations R1 and R2. In the remainder of the paper we will use simulation R2 due to its higher resolution in the intermediate density regions.

The time step on the zeroth level grid for the simulations, $\Delta\tau_0$, was set at the beginning of each global step to satisfy the Courant condition (with the Courant-Friedrichs-Lewy factor of $cfl = 0.4$) for cells on all levels and with the condition that the corresponding step in expansion factor would not exceed $\Delta a_0 \leq 0.003$ (the latter condition is usually imposed only during the early stages of evolution). The time steps for particles and cells on other levels were scaled appropriately: $\Delta\tau_l =$

$\Delta\tau_0 2^{-l}$. The simulations were started at $z = 30$ and a total of 364 global time steps were performed in both simulations.

4. Results

4.1. Spatial distribution of gas and dark matter

At the current epoch most of the mass ($\approx 7.5 \times 10^{14} h^{-1} M_\odot$) of the LSC is located in a filament roughly centered on the Virgo cluster and extending over $\sim 40 h^{-1} \text{Mpc}$. The simulated Local Group (LG) is located in an adjacent smaller filament, which is not a part of the main body of the LSC, and has a peculiar velocity of $\approx 250 \text{ km s}^{-1}$ toward the Virgo cluster. The peculiar velocity flow in the vicinity of the LG in the simulation is relatively “cold”: the peculiar line-of-sight velocity dispersion within $7 h^{-1} \text{Mpc}$ of the LG is $\lesssim 60 \text{ km s}^{-1}$, comparable to the observed velocity dispersion of nearby galaxies. In the main filament of the LSC, the peculiar velocities are higher with typical values of $\sim 200 - 300 \text{ km s}^{-1}$; the peculiar velocities are the highest, $\gtrsim 400 - 500 \text{ km s}^{-1}$ in the immediate vicinity of the Virgo cluster. The overall matter distribution and peculiar velocity field in the the simulated LSC region is discussed in detail in Paper I and we refer reader to this paper for further information. Here we will briefly discuss the distribution of gas and dark matter.

Figure 2 shows a $15 h^{-1} \text{Mpc}$ slice through the gas and DM distribution in the simulation R2. The slice is centered on the simulated Virgo cluster. The left panels show the (continuous) density field of gas (upper left panel) and distribution of DM particles (lower left panel). Comparison of the gas and DM distributions shows that at these large scales gas traces the gravitationally dominant DM distribution very well: similar filamentary structures and halos can be identified in both panels. As discussed above, the dominant structures are the “Virgo” cluster in the center and the horizontal filament around it. The right panels show the projected emission-weighted temperature field of the gas (upper panel) and projected density of the Warm-Hot (solid contours) and diffuse (dotted contour) phases of the gas. The panels show that warm ($\sim 10^5 - 10^6 \text{ K}$) gas is located in filaments, while hotter gas ($> 5 \times 10^6 \text{ K}$) is concentrated around virialized halos of groups and clusters. It

is the Warm-Hot gas that will be the main focus of our study.

Below we discuss properties and possible observational signatures of the intergalactic gas in the constrained simulations of the LSC region. The analysis presented below excludes the inner structure of the Virgo cluster. The cooling and feedback processes neglected in our simulations would affect the structure of the cluster. We will present a constrained simulation of the Virgo cluster that includes heating and cooling processes in a forthcoming paper.

4.2. Properties of gas

Davé et al. (2001) present a detailed discussion of gas properties in the currently favored structure formation models. They classify the gas in four phases: diffuse ($\delta < 1000$, $T < 10^5 \text{ K}$), condensed ($\delta > 1000$, $T < 10^5 \text{ K}$), hot ($T > 10^7 \text{ K}$), and warm-hot ($10^5 < T < 10^7 \text{ K}$), where δ and T are gas overdensity and temperature, respectively. The simulations presented here do not include cooling and thus cannot predict the fraction of gas in condensed phase, while fraction of gas in the hot phase is sensitive to the presence or absence of a small number of galaxy clusters in the simulation volume. However, the hot gas fraction is expected to be small ($\sim 5\%$) and the gas not in diffuse or WH phase should correspond approximately to the condensed fraction in the simulations with cooling. It is therefore interesting to compare the fraction of WH and diffuse gas to those in previous simulations. Davé et al. (2001) find that $\sim 40\%$ and $\sim 30\%$ of the gas at present epoch is in the diffuse and Warm-Hot (WH) phases, respectively. The fraction of WH gas appears to be rather robust: approximately the same fraction of WH gas is measured in simulations with and without cooling and/or supernova feedback. The corresponding fractions of diffuse and WH gas in the high-resolution region of our simulations are $\Omega_{\text{diff}}/\Omega_b \approx 0.41$ and $\Omega_{\text{WH}}/\Omega_b \approx 0.34$, respectively. Both fractions are in good agreement with the fractions found by Davé et al. (2001).

Figure 3 shows the X-ray volume emissivity in the $[0.5 - 2] \text{ keV}$ energy range and gas temperature as a function of gas density in the simulation R1. The points in the figure represent individual mesh cells randomly selected from the high-resolution

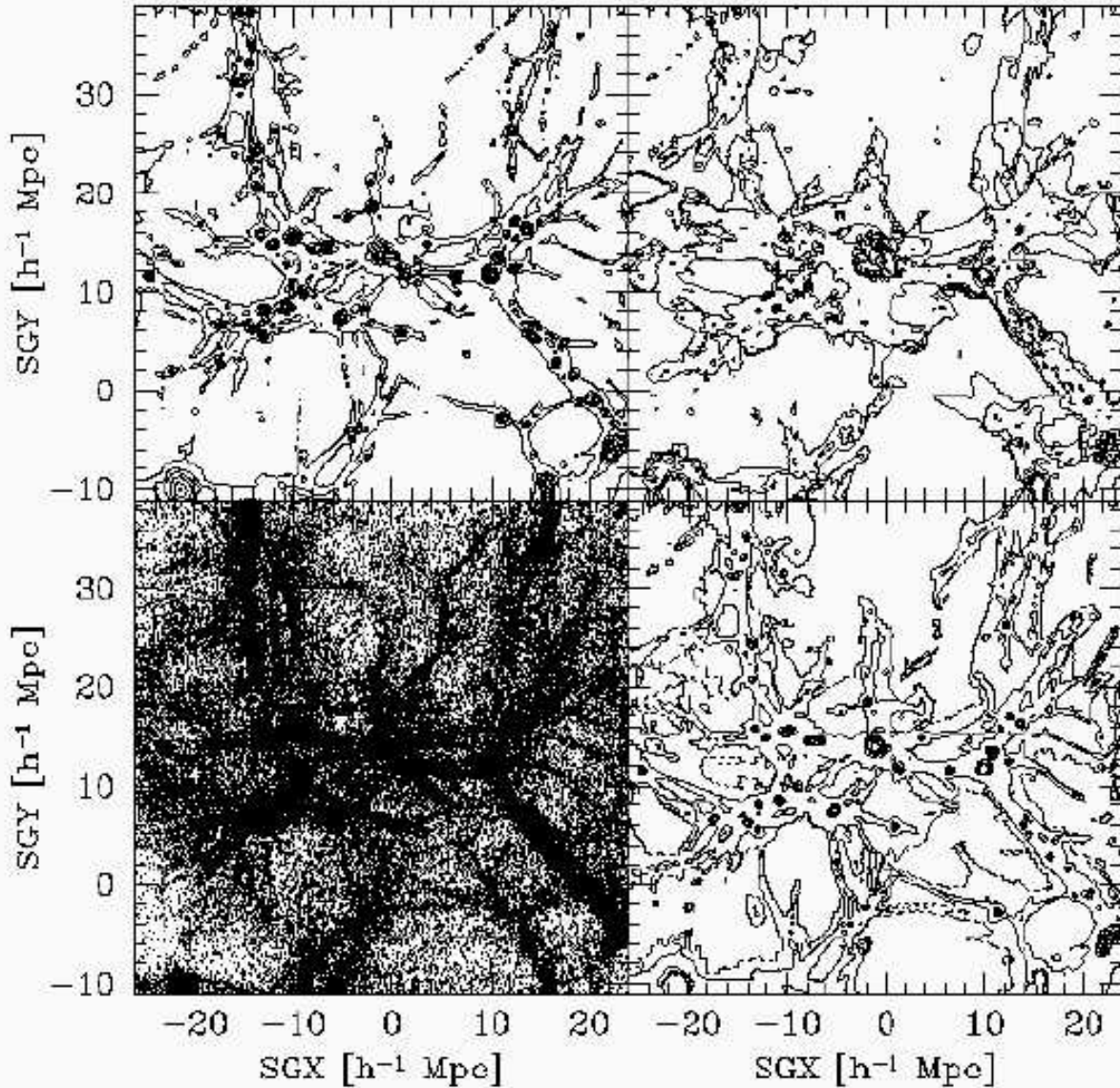


Fig. 2.— A slice through the gas and DM distribution in the simulation R2. The slice is centered on the simulated Virgo cluster and is $15h^{-1}\text{Mpc}$ thick. *Upper left panel:* the contour plot of the projected density field, where the thick solid contours correspond to the mean gas density, while subsequent contours correspond to the densities of 4, 8, 16, etc. times the mean density. *Lower left panel:* the distribution of DM particles in the slice; randomly selected subset of 10% of all the particles in the high-resolution region is shown. *Upper right panel:* the contour plot of the emission-weighted projected temperature field in the slice. The thick contour corresponds to temperature of 3×10^5 K, while other contours correspond to temperatures of 10^6 K, 4×10^6 K, 6×10^6 K, 8×10^6 K, and 10^7 K. *Lower right panel:* the projected density fields of the Warm-Hot (solid contours) and diffuse phases of the gas (dotted contour). The thick solid contour corresponds to the density of WHIM equal to the mean density of the gas, while thin solid contours correspond to the WHIM densities of 8, 16, 32, etc. times the mean gas density; the dotted contour corresponds to the density of diffuse gas equal to 0.1 of the mean gas density.

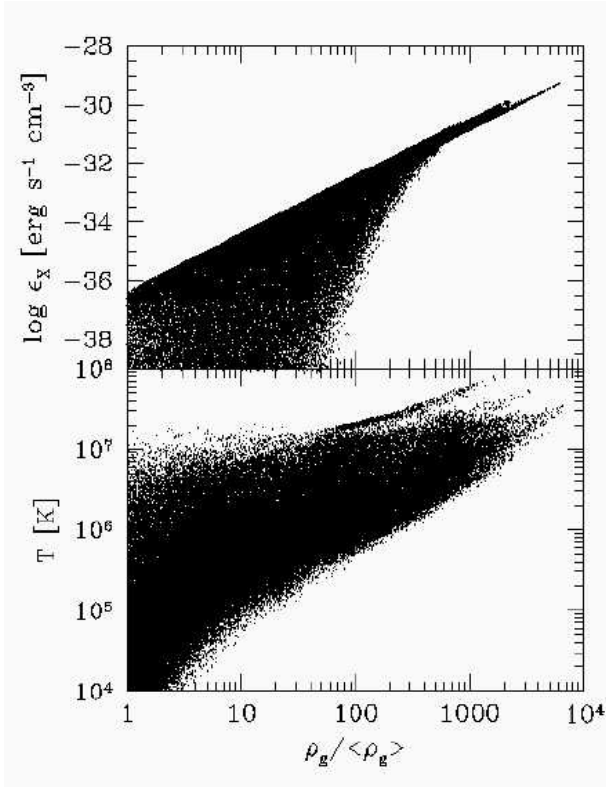


Fig. 3.— X-ray (0.5-2 keV) emissivity (*top panel*) and gas temperature (*bottom panel*) as a function of gas density. The gas density is given in units of the mean density. The X-ray emissivity was computed using the Raymond & Smith (1977) code assuming uniform metallicity of 0.3 solar. Points correspond to randomly selected individual mesh cells in the high-resolution simulation region. Note that the cells plotted correspond to relatively high-density regions and represent less than half of the volume; the median values of gas density, temperature, and X-ray emissivity by volume (i.e., half of the volume is at values below the median) are 0.29, 5000 K (the minimum assumed gas temperature), and 10^{-42} ergs $s^{-1} \text{cm}^{-3}$.

region of the simulation (see § 3). The X-ray emissivity was calculated using the Raymond & Smith (1977) code assuming complete ionization and uniform gas metallicity of 0.3 solar. Figure 3 shows that temperature is correlated with gas density, although there is much scatter (especially at low gas densities). As noted by Davé et al. (2001), the average can be roughly described as $\rho \propto T$. The large scatter in temperature translates into significant scatter in X-ray emissivities. The relatively

sharp upper edge in the $\epsilon_x - \rho_g$ scatter plot is due to the fact that at high temperatures (corresponding to the highest emissivities), the emissivity is a strong function of gas density ($\propto \rho_g^2$) and is a relatively weak function of temperature ($\propto T^{1/2}$). As can be seen from the lower panel, the maximum temperatures of the gas change by less than a factor of ten over four orders of magnitude in density. The upper envelope in the upper panel is therefore dominated by the density dependence: $\epsilon_x \propto \rho_g^2$ and scatter in temperature introduces only a small scatter at the maximum emissivity at a given ρ_g .

Note that although a large fraction of WH gas is at relatively low overdensities ($\rho_g / \langle \rho_g \rangle \lesssim 100$), the X-ray emission is dominated by gas at higher overdensities. Note also that at overdensities of $\rho_g / \langle \rho_g \rangle \sim 10$ most of the gas has temperatures in the range $T \sim 10^5 - 10^6$ K. The correlation of emissivity and temperature with density presented in Figure 3 are in good agreement with results of previous studies (Davé et al. 2001; Croft et al. 2001, see their Fig. 6 and Fig. 2, respectively).

4.3. Sky maps

The use of observational constraints implies that the computational box axis in our simulations are mapped with the same supergalactic coordinates as the observed universe. Because observational constraints small scales were not too tight, there was a room for fine-tuning the position of the origin of coordinates (i.e., position of the Local Group in the simulations). We choose the origin to be the location of a pair of galaxy size halos in the high-resolution dissipationless simulation described in Paper I (see Fig. 6 in that paper). For this choice of origin, the simulated Virgo cluster has supergalactic coordinates of $(SGX, SGY, SGZ) = -1.2, 13.7, 0.7 h^{-1} \text{Mpc}$ and is located $13.74 h^{-1} \text{Mpc}$ from the Local Group. Knowledge of the supergalactic coordinates allows us to construct sky maps in real celestial coordinates.

In the following we present a series of sky maps showing projections of various quantities in a region of the sky around the north galactic pole. The maps are shown as polar views in the galactic coordinates, with the North Galactic Pole (NGP; $b = 90^\circ$) in the center. We plot only a region

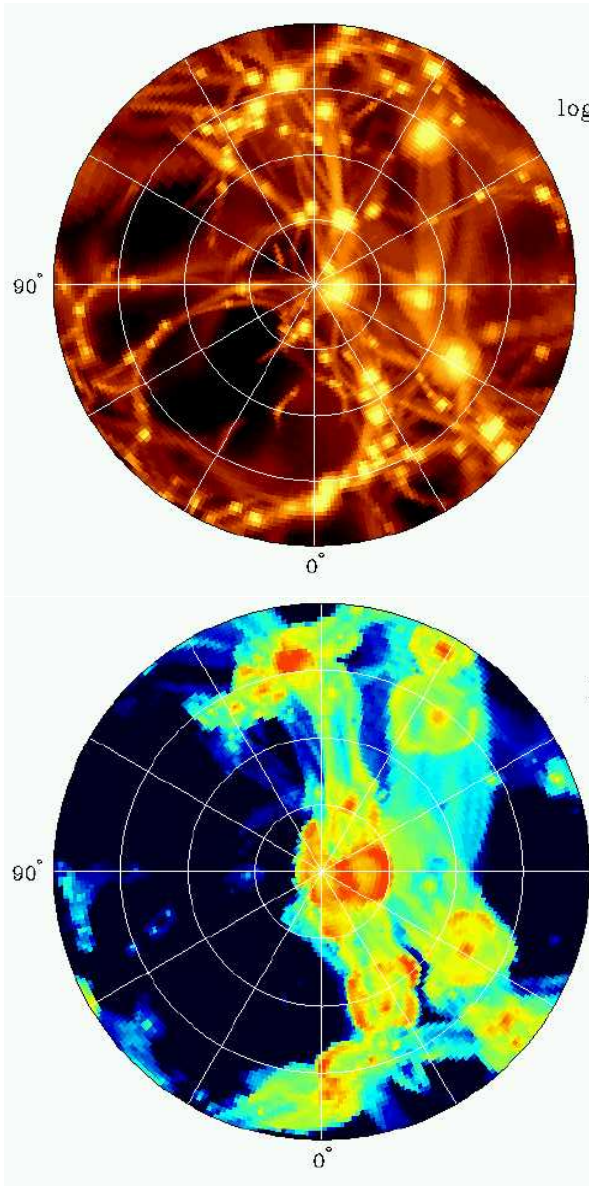


Fig. 4.— Sky maps of density (*top panel*) and X-ray emission weighted temperature (*bottom panel*) of the gas in the simulated Local Supercluster. The panels show polar views around the North Galactic Pole ($b > 30^\circ$). Radial lines and circles correspond to spacings of 30° and 15° in galactic l and b , respectively; $l = 0^\circ$ is at the bottom and $l = 90^\circ$ is on the left; $b = 90^\circ$ is in the center. The density represents the average maximum overdensity along a line of sight in a given map “pixel”; the temperature is in degrees Kelvin and is evaluated as an emission-weighted average along lines of sight in a “pixel” spanning from $2h^{-1}\text{Mpc}$ to $25h^{-1}\text{Mpc}$ from the origin. The corresponding color scales are shown by the bar to the right of each panel. The Virgo Cluster is close to the center of the plots; the Ursa Major cluster is close to the top of the plots. The Local Void is in the bottom left quadrant.

of $b > 30^\circ$. We do not consider other regions of sky because 1) most of the nearby structures in the high-resolution region ($\approx 30h^{-1}\text{Mpc}$ around the Virgo cluster) of the simulations are concentrated around the NGP (the Virgo cluster is located within 15° of the NGP) 2) the sky at low galactic latitudes is more difficult to observe due to galactic obscuration. All maps include only cells in the high-resolution region of the simulation; the resolution outside this region was considerably worse (cell size of $1.25h^{-1}\text{Mpc}$) and our predictions would be considerably less accurate. All quantities represent averages over a number of random lines of sight passing through each map pixel. The integration along lines of sight was done from $2h^{-1}\text{Mpc}$ to $25h^{-1}\text{Mpc}$. We thus exclude the regions in the immediate vicinity of the LG which are not modelled accurately in our simulations.

Figure 4 shows the sky maps of the gas overdensity and X-ray emission weighted temperature. Note that although the gas distribution is very filamentary in appearance, the overall distribution $\log(T_x)$ is flattened along a plane which is roughly aligned with the observed supergalactic plane. The large void in the lower left corner is the counterpart of the Local Void in the observed distribution of nearby galaxies. The temperature of gas in filaments ranges from one to a few million degrees K and reaches tens of million K within and around the virialized regions of groups and clusters. Note that these regions are surrounded by the narrow regions of enhanced temperature corresponding to accretion shocks. The accretion shocks are also visible around massive filaments. The two hottest regions in the center and at the top of the plot are the environments of the Virgo and Ursa Major clusters, respectively.

Figure 5 shows sky maps of surface brightness of X-ray emission in $[0.5 - 2]$ keV energy band and column densities of oxygen ions: OVI, OVII, and OVIII. The hot, $T \gtrsim 10^6$ K gas in filaments and virialized regions (see Figures 3 and 4) should emit soft X-ray radiation. As can be seen from the Figure 5, the X-ray surface brightness map has a more patchy appearance than both the density and temperature maps. This is because X-ray emission is roughly proportional to $\rho^2 T^{0.5}$ and is thus heavily weighted towards the highest density regions.

The emission-weighted average X-ray spectrum

from the considered sky region is shown in Figure 6. The spectrum was computed using the Raymond & Smith (1977) plasma code and assuming uniform gas metallicity of 0.3 solar. The model spectrum is compared to the broad-band measurements of soft X-ray extragalactic background from the RASS survey with the contribution of AGNs, stars, and the Local Hot Bubble subtracted (see Kuntz et al. 2001, for details). In both models and observations emission from the 3° region around the Virgo cluster was excluded. The figure shows that energies $\lesssim 0.5$ keV the predicted emission of the intergalactic gas is significantly lower than the measured background. As argued by Kuntz et al. (2001), this emission is likely due to the Milky Way’s own hot halo. However, at energies ~ 1 keV the X-ray emission of the intergalactic gas, although still relatively small ($\sim 10\%$ of observed background at these energies; the measured total background at 1 keV is $\sim 10 \text{ keV s}^{-1} \text{cm}^{-2} \text{sr}^{-1} \text{keV}^{-1}$), may be important for understanding the total background at these energies.

In addition to the X-ray brightness map, Figure 5 shows the sky maps of column densities of three ionic species of oxygen: OVI, OVII, and OVIII. The concentrations of these species were calculated using the current version (94.00) of the CLOUDY code (Ferland 2000) assuming that the gas is embedded in the observed XRB spectrum and has uniform metallicity of 0.3 solar. We assume that power-law XRB spectrum. $P(E) = AE^{-\Gamma}$, with $A = 9.5 \text{ keV s}^{-1} \text{cm}^{-2} \text{sr}^{-1} \text{keV}^{-1}$ (Kuntz et al. 2001) and $\Gamma = 1.46$ (Chen et al. 1997); this is equivalent to the flux $J_\nu = 1.2 \times 10^{-26} (\nu/\nu_X)^{-0.46} \text{ ergs s}^{-1} \text{cm}^{-2} \text{sr}^{-1} \text{Hz}^{-1}$, where $h\nu_X = 40 \text{ keV}$. We also assume that the spectrum has an exponential cutoff at energies above $h\nu_X$ and at very small energies ($\ll 1 \text{ keV}$).

Comparison of the column density maps in Figure 5 to the projected density map in Figure 4 shows that high column density regions are roughly correlated with regions of high gas density. Note, in particular, that high-column density regions are in general located near the supergalactic plane. Nevertheless, different ionic species trace regions of somewhat different densities and temperatures (e.g. Hellsten et al. 1998; Nahar 1999) and their maps, therefore, differ in details. For instance, the column densities of OVI and OVII

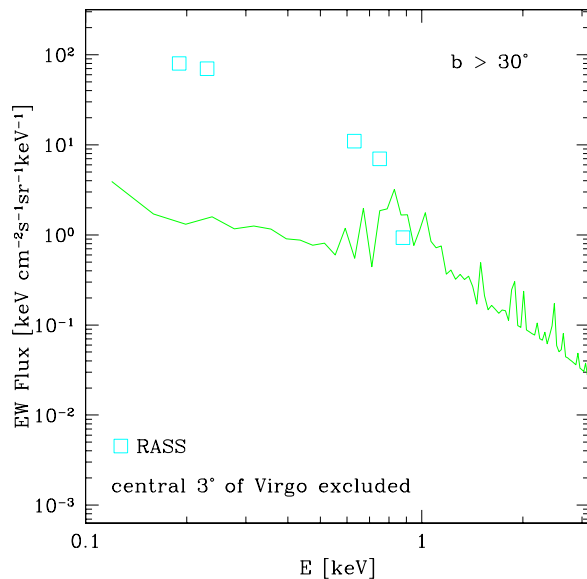


Fig. 6.— The X-ray spectrum of gas in the LSC region. The spectrum, shown by the green solid line, represents the emission-weighted average over the sky region around the NGP ($b > 30^\circ$) shown in Figure 5. Open squares show the broad-band measurements of the intensity of the X-ray background by the RASS with known contributions of AGNs, stars, and the Local Hot Bubble subtracted (Kuntz et al. 2001). The 3° region around the center of the Virgo cluster was excluded in both model and observations.

are depressed in the vicinity of the Virgo cluster ($l \sim 300^\circ$, $b \sim 85 - 90^\circ$) due to the high gas temperatures around the Virgo cluster. The decrease in column density of OVIII in this region is relatively small.

Our primary interest is evaluating the prospects of detection of the gas in the LSC region. The oxygen is the most abundant of the metals that can absorb or emit in UV and X-rays. The absorption or emission by lines of the ionic species of oxygen is therefore the most promising probe of the LSC gas. The strongest lines of OVII and OVIII are in soft X-rays at 0.5740 keV and 0.6536 keV, respectively. The OVI can be detected using resonance line doublet in UV at $\lambda\lambda 1031.92, 1037.62 \text{ \AA}$. The current instruments in X-ray (*Chandra* and *XMM-Newton*) and UV (*FUSE*) are sufficiently sensitive to detect at least some of the intergalactic gas. The exact detection limit depends on

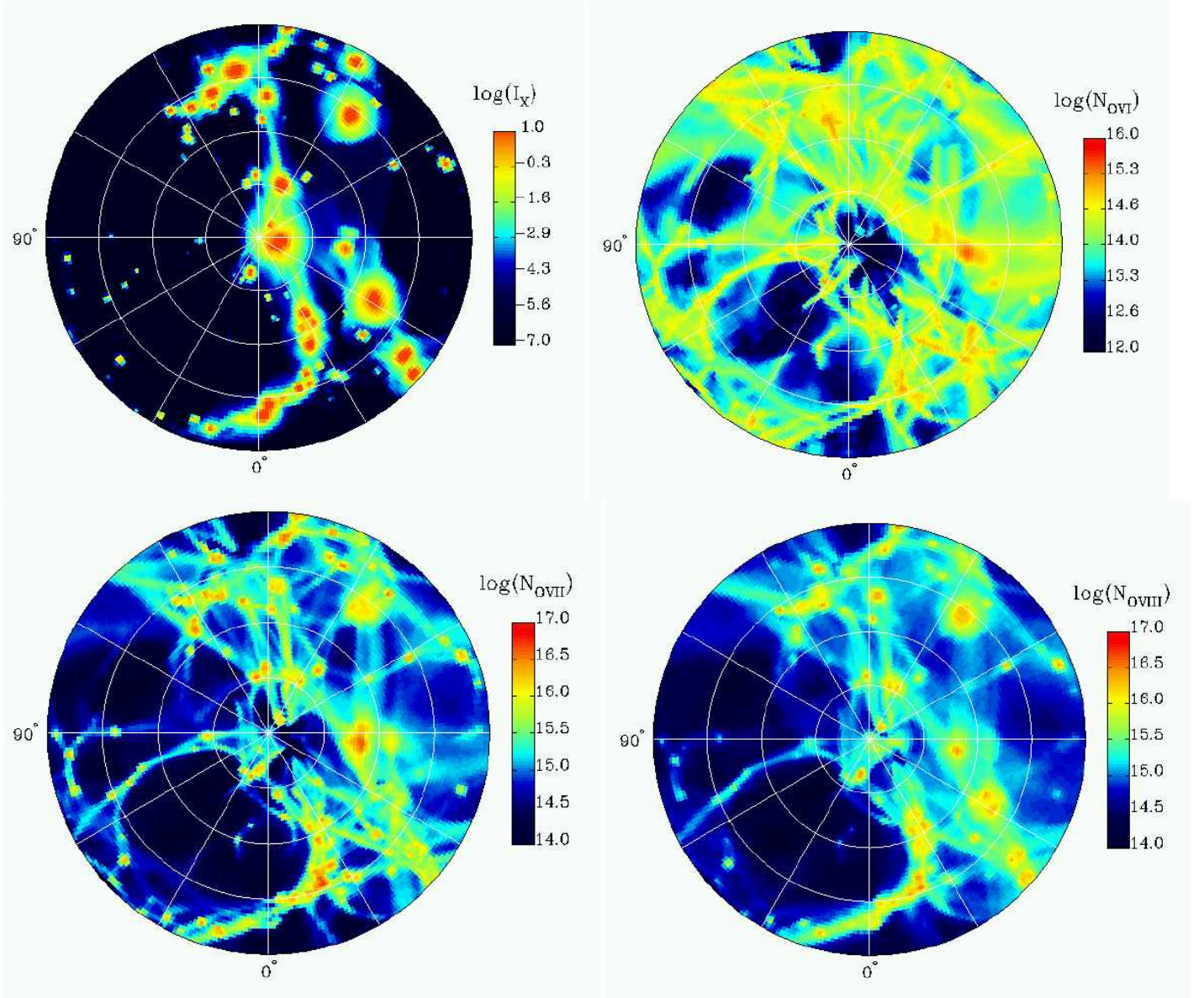


Fig. 5.— Sky maps of X-ray surface brightness in $[0.5 - 2]$ keV (*top left*) and column densities of oxygen ions: OVI (*top right*), OVII (*bottom left*), and OVIII (*bottom right*). The X-ray brightness is given in $\text{keVs}^{-1}\text{cm}^{-2}\text{sr}^{-1}\text{keV}^{-1}$, while column densities are in cm^{-2} . The layout is similar to that of Figure 4. The brightness and column densities were evaluated by averaging along random lines of sight within each map “pixel” in the distance range $[2, 25]h^{-1}\text{Mpc}$. See text for details.

the brightness of the background source (in the case of absorption) and specifics of the instrument and observation (time of integration, spectral resolution, etc.). For an X-ray bright quasar and a reasonable integration time (100 ks), the Fang & Canizares (2000) estimate that *Chandra*, *XMM*, and the planned *Constellation-X* should detect OVIII (sensitivity to OVII is similar) at column densities higher than 3.5×10^{16} , 7.6×10^{15} , and $1.3 \times 10^{15} \text{ cm}^{-2}$, respectively. The OVI was robustly detected in absorption with *FUSE* for column densities $\gtrsim 10^{14} \text{ cm}^{-2}$ (Tripp et al. 2000).

The column density maps in Figure 5 show that for the assumed metallicity the column densities of OVI should be detectable with *FUSE* over a large fraction of the sky, especially near the supergalactic plane. On the other hand, the column densities of OVII and OVIII detectable with *Chandra* and *XMM-Newton* cover a much smaller fraction of the sky. This fraction is much higher for the sensitivity of the *Constellation-X*.

The cumulative fraction of the sky (estimated over the region of the sky shown in Figure 5, i.e. at $b > 30^\circ$) at column densities above a given value is shown in Figure 7. This fraction can be thought of as a probability to have a detectable column density in a random line of sight. The figure shows predictions under three different models for gas metallicity: uniform metallicity of 0.05 and 0.3 solar, and density-dependent law,

$$Z/Z_\odot = 0.025(\rho_g/\langle\rho_g\rangle)^{0.35}, \quad (1)$$

which approximates results of numerical simulations of Cen & Ostriker (1999a). For uniform metallicity of $Z/Z_\odot = 0.3$, the probability is ≈ 0.5 for the detection of OVI absorption with *FUSE*. The OVIII absorption (results for OVII are quantitatively similar) should be detected with the probability of ≈ 0.5 with *Constellation-X* and $\lesssim 0.05$ with the *XMM-Newton* and *Chandra*. For lower metallicities of the gas, the probabilities are considerably lower. Note that sky fraction distributions for the density-dependent metallicity are similar to the uniform metallicity of $Z/Z_\odot = 0.05$. This indicates that the signal is dominated by gas at overdensities of $\sim 5 - 10$ (see eq. 1) and is sensitive to the average metallicity of this gas. Note that the fractions are calculated over the entire sky region around the NGP ($b > 30^\circ$), which includes sizeable voids in the gas density; the fractions will

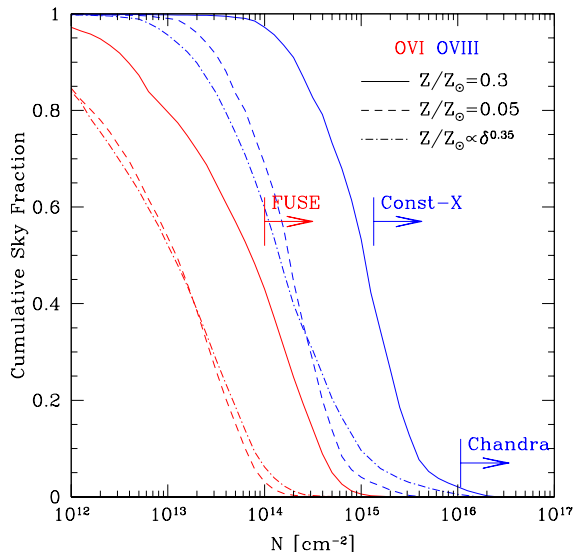


Fig. 7.— The fraction of the sky around the NGP ($b > 30^\circ$) at column densities greater than a given value N for OVI and OVIII for different metallicity models. The results for OVII are quantitatively similar to those for OVIII. The *solid* and *dashed* lines show results for the uniform metallicity of gas of 0.3 and 0.05 solar, respectively; the *dot-dashed* shows results for the density-dependent metallicity of the gas: $Z/Z_\odot = 0.025\delta_g^{0.35}$, where δ_g is gas overdensity, which approximates results of numerical simulations of Cen & Ostriker (1999a). The sensitivity of current and future instruments is also shown (sensitivity of the *XMM-Newton* is intermediate to those of *Constellation-X* and *Chandra*). Note that for the metallicity of the IGM of 0.3 solar, OVI and OVII/OVIII have column densities detectable with the *FUSE* and *Constellation-X* over a large fraction of this sky region.

be higher if one focuses on the sky regions near the supergalactic plane.

5. Discussion and conclusions

We presented results of high-resolution gas dynamics+ N -body cosmological simulations of the Local Supercluster region constrained to reproduce the observed nearby large-scale density field. The simulations focused on the region of $\approx 30h^{-1}\text{Mpc}$ around the Virgo cluster and followed the dynamics of dissipationless dark matter and adiabatic dynamics of gas using the new version of the Adaptive Refinement Tree code that

includes gasdynamics. The detailed discussion of constrained simulations, setup of initial conditions, and properties of the density and velocity fields in the simulated Local Supercluster are presented in a separate paper (Klypin et al. 2001a). In this paper we use the simulations to study the properties and possible observational signatures of intergalactic medium in the LSC region. We find that within $30h^{-1}\text{Mpc}$ of the Virgo cluster $\approx 30\%$ of baryons is in the warm/hot phase at $T \sim 10^5 - 10^7$ K and $\approx 40\%$ are in the diffuse phase ($T < 10^5$ K, $\delta < 1000$). The latter phase occupies most ($\gtrsim 90\%$) of the volume.

We presented simulated sky maps of $0.5 - 2$ keV X-ray surface brightness and column densities of three ionic species of oxygen (OVI, OVII, and OVIII). The maps are constructed in real galactic coordinates for the sky region around the North Galactic Pole ($b > 30^\circ$). The map of X-ray brightness has a patchy appearance with most of the emission coming from the high-density environments of groups and clusters. We compared emission-weighted average X-ray spectrum from the warm/hot gas in the simulation (Figure 6) to the measurements of soft X-ray background (Kuntz et al. 2001). The predicted flux at energies $\lesssim 0.5$ keV is 10 to 100 times lower than the observed flux. The LSC gas therefore cannot explain this soft X-ray emission which is likely to be associated with the hot halo of the Milky Way. At energies around 1 keV, the predicted flux constitutes $\approx 5 - 10\%$ of the total XRB flux and is therefore an important component of the XRB at these energies. At higher energies, the contribution of the LSC gas to the XRB is insignificant. It is not clear whether the X-ray emission of the intergalactic gas can be reliably detected in the near future. Such detection is difficult because one needs a survey that covers a large sky area and is sufficiently sensitive to detect the signal only $\sim 1\%$ of the XRB. The diffuse LSC emission should be correlated with the supergalactic plane, but so is the X-ray emission from nearby AGNs (Shaver & Pierre 1989).

Recently, Boughn (1999) analyzed the *HEAO 1* full sky $2 - 10$ keV X-ray map and found evidence for the “diffuse” (unresolved) X-ray emission associated with the supergalactic plane. The quoted maximum surface brightness of the diffuse emission constitutes about 1% of the $2 - 10$ keV

XRB and is $I_X \approx 5 \times 10^{-10}$ ergs $\text{s}^{-1}\text{cm}^{-2}\text{sr}^{-1}$ (see his Table 1). This corresponds to ≈ 0.04 keV $\text{s}^{-1}\text{cm}^{-2}\text{sr}^{-1}\text{keV}^{-1}$ assuming that flux is constant over $2 - 10$ keV. This flux is consistent with the predicted flux from the WH gas in our simulation (see Fig. 6): $10^{-2} - 10^{-1}\text{keV s}^{-1}\text{cm}^{-2}\text{sr}^{-1}\text{keV}^{-1}$ at energies $2 - 5$ keV (i.e., $\approx 0.1 - 1\%$ of the total XRB at these energies; see Kuntz et al. 2001); the flux decreases steeply at higher energies.

As can be seen from the X-ray brightness map in Figure 5, most of the X-ray emission is indeed concentrated towards the supergalactic plane. However, the emission is patchy and is far from being uniform. In contrast, Boughn (1999) modelled the gas distribution using a simple “pillbox” model for the distribution of gas in the LSC region: the uniform gas distribution within a disk of radius R_{SC} and thickness $H_{\text{SC}} \approx 0.25R_{\text{SC}}$. For the detected diffuse X-ray flux this model implies gas density of $2.5 \times 10^{-6} \text{cm}^{-3}$ for temperatures of around 10 keV. This temperature is much higher than the typical temperatures of the LSC gas in our simulation. The difference is due to the fact that the gas distribution in the simulated LSC is not described by the pillbox model. As can be seen from Figures 4 and 5, the distribution of matter in the LSC region is filamentary rather than disk-like and the X-ray emission is far from being uniform. The bulk of the X-ray emission thus comes from the relatively high-density, $n_e \sim 10^{-5} - 10^{-3} \text{cm}^{-3}$, regions within and around groups and clusters.

The hot and dense regions of the LSC should also distort the cosmic microwave background radiation via the inverse Compton or Doppler scattering, the thermal and kinetic Sunyaev-Zel’dovich effect, respectively (SZ; Sunyaev & Zeldovich 1980, and references therein). The temperature fluctuations of the CMB due to the non-relativistic thermal SZ effect can be written as:

$$\frac{\Delta T}{T} = y \left(\frac{e^x + 1}{e^x - 1} - 4 \right), \quad (2)$$

where $x \equiv hv/kT_{\text{CMB}}$, $y = 1.117 \times 10^{-34} \int n_e T_e dl$ (all quantities are in cgs units and the integral is along line-of-sight). In the Rayleigh-Jeans regime ($hv \ll kT_{\text{CMB}}$): $\Delta T/T \approx 2y$; the deviation of CMB temperature along a given direction is thus proportional to the gas pressure integrated along this direction.

Although for temperatures and densities typical for the gas in the LSC the SZ effect is not expected to be very strong, due to the large angular extent of the LSC, it should contribute to the anisotropy on the on the angular scales of $\sim 1 - 10^\circ$. The thermal SZ map has patchy appearance similar to that of the X-ray brightness in Figure 5 with $\Delta T/T \sim 5 \times 10^{-6} - 10^{-5}$ within groups and clusters, $\sim 10^{-7}$ on their outskirts, and $\sim 10^{-8}$ in the strongest filaments. The kinetic SZ effect has similar magnitude. These fluctuations are small and are below current sensitivity limits of the SZ observations; their contribution to the large angular scale anisotropies measured by COBE satellite is insignificant.

Finally, we presented (Figure 5) sky maps of column densities of the three ionic species of oxygen: OVI, OVII, and OVIII. The column densities were calculated using the densities and temperatures of gas in the high-resolution region of the simulation and assuming the uniform metallicity of 0.3 solar and the observed X-ray background. Although, the OVI is the least abundant (its abundance is more than an order of magnitude smaller than abundances of OVII and OVIII) of the three ions, absorption or emission in its resonant doublet at $\lambda\lambda 1031.92, 1037.62 \text{ \AA}$ offers *currently* the best prospect for detection of the warm/hot intergalactic gas in the LSC region. For the assumed metallicity of the IGM, our simulations predict that the probability to have a column density of OVI detectable with FUSE along a random line of sight in the northern galactic hemisphere is $\gtrsim 0.5$; the probability is higher in the regions of the sky close to the supergalactic plane.

Our predictions would be affected if metallicity in filaments is significantly smaller than 0.3 solar (the metallicities observed in the virialized regions of clusters). However, there are good reasons to believe that the filaments should be enriched to the levels comparable to the intracluster medium. The observations of metals in the Lyman alpha forest at high redshifts indicates that regions with overdensities of ~ 10 (corresponding to filaments) have metallicities in the range $10^{-3} - 10^{-2}$ solar (see, e.g., Cowie & Songaila 1998; Schaye et al. 2000). The simulations predict a steep dependence of metallicity on the density in this regime with metallicity quickly reaching values of ~ 0.1 solar in the vicinity of the virialized regions (e.g.,

Gnedin 1998; Cen & Ostriker 1999a; Aguirre et al. 2001). As the Universe evolves, the metallicity in the low-density regions is expected to increase steadily (Cen & Ostriker 1999a). At $z = 0$, numerical simulations of Cen & Ostriker (1999a) predict the average metallicity of $\sim 0.05 - 0.1$ solar (with a significant scatter around the average) for overdensities of ~ 10 ; their results can be approximated by the density-dependent metallicity given by equation 1. Figure 7 shows that our results are sensitive not to the particular density dependence of metallicity but to the average metallicity of gas at overdensities $\approx 1 - 10$. Detections (or lack thereof) of oxygen absorption within the Local Supercluster should therefore provide useful constraints on the $z = 0$ metallicity of IGM in filaments.

Although the structures in the simulation reproduce the large-scale density field rather well, we expect certain differences with the real observed structures. For example, the simulated Virgo cluster is displaced by several degrees from the location of the real Virgo. We cannot thus reliably predict the column density in any specific direction. However, viewed statistically, our results suggest that for a sample of background sources distributed over the northern sky, about half of the lines of sight should pass through the column density $\gtrsim 10^{14} \text{ cm}^{-2}$. Unfortunately, the probability decreases steeply for higher column densities ($\approx 10\%$ for $N_{\text{OVI}} \gtrsim 4 \times 10^{14} \text{ cm}^{-2}$). We predict that OVI column density is very low in the area of $\approx 10^\circ$ around the Virgo cluster. This prediction is only for the IGM; the halos of individual galaxies in or around Virgo may cause OVI absorption. The OVI absorption of the intergalactic gas should be easy to separate from the local absorption in the Milky Way: most of the absorbing gas should be redshifted by $\sim 3 \pm 2 \times 10^{-3}$. The typical absorption should also be fairly broad as the typical line of sight peculiar velocities of gas in the high density regions are $\sim 100 - 400 \text{ km s}^{-1}$ (see Figs. 5 and 6 in Paper I).

The absorption lines of OVII and OVIII in soft X-rays will be difficult to detect with current instruments. The predicted probability for absorption detectable with *Chandra* or *XMM-Newton* is $\lesssim 5\%$ for a random line of sight in the north-

ern galactic sky. For the planned *Constellation-X*⁵ mission the probability is an order of magnitude higher. The simulations predict that regions of the highest column densities of OVII and OVIII correspond to the high-density regions in and around galaxy groups (see Fig. 5).

We would like to point out that our predictions are made under the assumptions negligible cooling and absence of significant heating of the intergalactic gas. We think that effects of cooling should not have a significant effect on our predictions for the oxygen ion column densities. The cooling time is sufficiently short only in the high density regions which would occupy a very small fraction of the sky and thus would not affect the cumulative distribution of column densities. Comparison of adiabatic simulation to the simulations that include cooling and stellar feedback presented by (Davé et al. 2001) shows that the fraction of baryons in the warm/hot intergalactic medium (that causes most of the absorption) is not sensitive to the inclusion of additional physics. Note, however, that the effects of feedback in these simulations are much smaller than in the extreme feedback models that assume a uniform preheating of the intergalactic gas with energy of order of 1 keV per particle in order to explain the observed correlation of cluster X-ray luminosities and temperatures. Such feedback would affect the gas evolution and its spatial distribution lowering gas density in groups and poor clusters and completely destroying most of the filaments. However, we believe that there is no compelling evidence that the uniform preheating actually occurred. Moreover, the existence of Lyman alpha forest at high and low redshifts argues against such extreme uniform feedback.

The results presented in this paper are only one example of useful application of the constrained simulations. In Paper I we addressed the problem of the coldness of the observed local peculiar velocity field of galaxies and showed that the properties of the local flow can be well reproduced in the currently popular Λ CDM cosmology. The constrained simulations are unique because they allow properties of individual simulated structures to be compared to the properties of their real counterpart. As a first step in this direction, we are

currently carrying out high-resolution constrained simulations of the Virgo cluster in the Λ CDM cosmology. The simulated cluster forms in the environment very similar to the real Virgo. The differences in the properties and internal structure of the simulated and observed clusters should thus give us clues about the physical processes shaping the evolution of intracluster gas. Another very interesting application of the constrained N -body+gasdynamics simulations would be predictions on the spatial distribution of the local Lyman alpha forest. These predictions could be compared to and provide interpretation for the observed large-scale distribution of the nearby Lyman alpha absorbers (e.g. Stocke et al. 2000). We conclude that the constrained simulations of the type presented here should have many other useful applications in comparisons of model predictions with various observations of the nearby Universe.

We would like to thank Alexei Khokhlov for providing us with his Godunov solver and very useful discussions during the initial stages of code development and David Weinberg for useful discussions and suggestions during the course of this project. We acknowledge support from the grants NAG-5-3842 and NST-9802787. A.V.K. was supported by NASA through Hubble Fellowship grant from the Space Telescope Science Institute, which is operated by the Association of Universities for Research in Astronomy, Inc., under NASA contract NAS5-26555. Y.H. has been supported in part by the Israel Science Foundation (103/98). AAK and AVK thank the Institute of Astronomy at Cambridge in the spring of 2001 for hospitality and support during their visit where the major portion of this project was completed. Computer simulations presented in this paper were done on the Origin 2000 at the National Center for Supercomputing Applications (NCSA) at Urbana-Champaign.

REFERENCES

- Abel, T., Bryan, G. L., & Norman, M. L. 2000, *ApJ*, 540, 39
- Aguirre, A., Hernquist, L., Schaye, J., Katz, N., & Weinberg, D. H. 2001, *astro-ph/0105065*
- Aldcroft, T., Elvis, M., McDowell, J., & Fiore, F. 1994, *ApJ*, 437, 584

⁵<http://constellation.gsfc.nasa.gov/>

- Basko, M. M., Komberg, B. V., & Moskalenko, E. I. 1981, *AZh*, 58, 701
- Bistolas, V. & Hoffman, Y. 1998, *ApJ*, 492, 439+
- Boughn, S. P. 1999, *ApJ*, 526, 14
- Cen, R. & Ostriker, J. P. 1999a, *ApJ*, 519, L109
- . 1999b, *ApJ*, 514, 1
- Chen, L. ., Fabian, A. C., & Gendreau, K. C. 1997, *MNRAS*, 285, 449
- Colella, P. & Glaz, H. M. 1985, *J. Comp. Phys.*, 59, 264
- Cowie, L. L. & Songaila, A. 1998, *Nature*, 394, 44
- Croft, R., Di Matteo, T., Davé, R., Hernquist, L., Katz, N., Fardal, M., & Weinberg, D. 2001, *astro-ph/0010345*
- Davé, R., Cen, R., Ostriker, J. P., Bryan, G. L., Hernquist, L., Katz, N., Weinberg, D. H., Norman, M. L., & O'Shea, B. 2001, *ApJ*, 552, 473
- Davé, R., Hernquist, L., Katz, N., & Weinberg, D. H. 1999, *ApJ*, 511, 521
- Fang, T. & Canizares, C. R. 2000, *ApJ*, 539, 532
- Fang, T., Marshall, H., Bryan, G., & Canizares, C. 2001, *astro-ph/0102370*
- Ferland, G. J. 2000, in *Revista Mexicana de Astronomia y Astrofisica Conference Series*, Vol. 9, 153–157
- Frenk, C. S., White, S. D. M., Bode, P., Bond, J. R., Bryan, G. L., Cen, R., Couchman, H. M. P., Evrard, A. E., Gnedin, N., Jenkins, A., Khokhlov, A. M., Klypin, A., Navarro, J. F., Norman, M. L., Ostriker, J. P., Owen, J. M., Pearce, F. R., Pen, U. ., Steinmetz, M., Thomas, P. A., Villumsen, J. V., Wadsley, J. W., Warren, M. S., Xu, G., & Yepes, G. 1999, *ApJ*, 525, 554
- Fukugita, M., Hogan, C. J., & Peebles, P. J. E. 1998, *ApJ*, 503, 518
- Ghigna, S., Moore, B., Governato, F., Lake, G., Quinn, T., & Stadel, J. 2000, *ApJ*, 544, 616
- Gnedin, N. Y. 1998, *MNRAS*, 294, 407+
- Hellsten, U., Gnedin, N. Y., & Miralda-Escudé, J. 1998, *ApJ*, 509, 56
- Hoffman, Y. & Ribak, E. 1991, *ApJ*, 380, L5
- Khokhlov, A. 1998, *J. Comp. Phys.*, 143, 519
- Khokhlov, A. M., Höflich, P. A., Oran, E. S., Wheeler, J. C., Wang, L., & Chtchelkanova, A. Y. 1999, *ApJ*, 524, L107
- Klypin, A., Hoffman, Y., Kravtsov, A., & Gottlöber, S. 2001a, submitted, *astro-ph/0107104*
- Klypin, A. A., Kravtsov, A. V., Bullock, J. S., & P., P. J. 2001b, in press, *astro-ph/0006343*
- Knebe, A., Kravtsov, A. V., Gottlöber, S., & Klypin, A. A. 2000, *MNRAS*, 317, 630
- Kolatt, T., Dekel, A., Ganon, G., & Willick, J. A. 1996, *ApJ*, 458, 419+
- Kravtsov, A. V. 1999, PhD thesis, New Mexico State University
- Kravtsov, A. V., Klypin, A. A., & Khokhlov, A. M. 1997, *ApJS*, 111, 73+
- Kuntz, K. D., Snowden, S. L., & Mushotzky, R. F. 2001, *ApJ*, 548, L119
- Martel, H. & Shapiro, P. R. 1998, *MNRAS*, 297, 467
- Nahar, S. N. 1999, *ApJS*, 120, 131
- Norman, M. L. & Bryan, G. L. 1999, in *ASSL Vol. 240: Numerical Astrophysics*, 19+
- Perna, R. & Loeb, A. 1998, *ApJ*, 503, L135
- Phillips, L., Ostriker, J., & Cen, R. 2001, *astro-ph/0011348*
- Plewa, T. & Müller, E. 2001, submitted, *astro-ph/0010626*
- Raymond, J. C. & Smith, B. W. 1977, *ApJS*, 35, 419
- Refregier, A. & Teyssier, R. 2001, submitted, *astro-ph/0012086*
- Reimers, D., Baade, R., Hagen, H.-J., & Lopez, S. 2001, *astro-ph/0106097*

- Ricker, P. e. a. 2001, astro-ph/0011502
- Schaye, J., Rauch, M., Sargent, W. L. W., & Kim, T. 2000, ApJ, 541, L1
- Shandarin, S. F. 1980, Astrophysics, 16, 439
- Shapiro, P. R. & Bahcall, J. N. 1980, ApJ, 241, 1
- Shaver, P. A. & Pierre, M. 1989, A&A, 220, 35
- Stoche, J. T., Shull, J. M., Penton, S. V., Gibson, B. K., Giroux, M. L., & McLin, K. M. 2000, astro-ph/0009190
- Sunyaev, R. A. & Zeldovich, I. B. 1980, ARA&A, 18, 537
- Tripp, T. M. & Savage, B. D. 2000, ApJ, 542, 42
- Tripp, T. M., Savage, B. D., & Jenkins, E. B. 2000, ApJ, 534, L1
- Truelove, J. K., Klein, R. I., McKee, C. F., Holliman, J. H., Howell, L. H., Greenough, J. A., & Woods, D. T. 1998, ApJ, 495, 821+
- van de Weygaert, R. & Hoffman, Y. 1999, in Evolution of Large Scale Structure : From Recombination to Garching, 178+
- van Leer, B. 1979, J. Comp. Phys., 32, 101
- Voit, G. M. & Bryan, G. L. 2001, ApJ, 551, L139